

Self-optimized contact in air-robust thermoelectric junction towards long-lasting heat harvesting

Received: 2 December 2024

Accepted: 5 February 2025

Published online: 10 February 2025

 Check for updatesAiran Li^{1,3}, Longquan Wang^{1,2,3}, Jiankang Li^{1,2}, Xinzhi Wu¹ & Takao Mori^{1,2} 

Ensuring long-term reliable contacts in thermoelectric devices is particularly challenging due to their operation under high temperatures and has been one of the large obstacles in the field for application. Typically, thermodynamically driven atomic diffusion and reactions often degrade the contacts, leading to increased contact resistivity and ultimately limiting the device's lifespan. Here, we report an unconventional self-optimized contact resistivity mechanism in the Sb/MgAgSb junction. Mg diffusion from MgAgSb to Sb does not degrade but instead optimizes its contact resistivity even after aging in air for 30 days. This unexpected automatic optimization arises from an increased carrier concentration in MgAgSb, which enhances electron tunneling across the interface, effectively reducing the contact resistivity. Leveraging the self-optimized contact in Sb/MgAgSb and stable thermoelectric performance of MgAgSb, a two-pair thermoelectric device employing 100-day air-aged Sb/MgAgSb achieves an impressive conversion efficiency of 8.1% and a rare power density of 0.41 W cm⁻² under 294 K temperature gradient. These results underscore its significant potential for robust, long-term heat harvesting. The self-optimization mechanism identified in this work also offers valuable insights for designing future junctions for high-temperature applications.

Metal-semiconductor contacts are essential in electronic systems due to their critical role in controlling the flow of electrical signals at the interface^{1,2}. The energy barriers formed between the metal and semiconductor typically determine whether the contact behaves as a rectifying or ohmic junction, directly influencing current flow, power consumption, and device efficiency, particularly in transistors, diodes, and thermoelectrics^{3–6}. Thermoelectric (TE) devices, which enable the direct conversion of heat into electricity based on the Seebeck effect, offer great potential for sustainably powering numerous sensors in the Internet of Things (IoT) and contributing to carbon-neutral goals via waste heating energy harvesting^{7–9}. As global energy demand continues to rise, leveraging waste heat presents a significant opportunity to improve energy efficiency, underscoring the importance of advancing TE technologies to enhance energy utilization. However, unlike most electronic devices that typically operate around room

temperature, TE devices usually function under high temperatures and their gradients, which demands that TE materials and numerous contacts within the device endure harsh conditions for extended periods without obvious performance degradation^{10,11}.

The performance of TE materials is typically evaluated by the dimensionless figure of merit, $zT = S^2\sigma T/\kappa$, where S is the Seebeck coefficient, σ is electrical conductivity, T is the absolute temperature and κ is thermal conductivity. Significant progress has been made with the development of high-performance TE materials, advancing TE technology in both power generation and solid-state cooling^{12–19}. However, for practical applications, the stability of TE materials under high temperatures, electric fields and their gradient is just as critical as the materials' performance. At elevated temperatures or under strong electric fields, issues such as element evaporation, environmental reactions, and ion migration can degrade the performance of TE

¹Research Center for Materials Nanoarchitectonics (MANA), National Institute for Materials Science (NIMS), Tsukuba, Japan. ²Graduate School of Pure and Applied Sciences, University of Tsukuba, Tsukuba, Japan. ³These authors contributed equally: Airan Li, Longquan Wang. ✉ e-mail: MORI.Takao@nims.go.jp

materials, hindering their practical use^{20–23}. In addition to the TE materials themselves, ensuring the stability of contacts between TE materials and electrodes poses an even greater difficulty.

Contacts always involve materials with differing chemical compositions, which often leads to thermodynamic atomic diffusion and reaction, especially under high temperatures and their gradients. This atomic diffusion and reaction alter the contact properties and often degrades the device's performance^{24–31}. To mitigate atomic diffusion and reaction, TE interface materials (TEiM) are commonly used in fabricating TE legs, forming a “TEiM/TE material/TEiM” sandwiched structure with two junctions on either side^{32–34}. Generally, TEiMs are selected from metals or alloys due to their high σ and κ , which help minimize energy loss during heat and electricity transport. Since TE materials are typically semiconductors, metal-semiconductor contacts are formed between TEiMs and TE materials. In addition to the σ and κ of TEiMs, establishing ohmic contacts with low contact resistivity ρ_c between TEiMs and TE materials is crucial.

When considering ρ_c in TEiM/TE material, the effective TE performance will shift from the material's zT to $zT_{\text{eff}} = zT \times L/(L + 2\rho_c\sigma)$, where L is the length of TE leg^{35–37}. According to this formula, high ρ_c will degrade the performance of the TE leg and device. Therefore, it is essential to achieve low ρ_c , especially the long-term low ρ_c between TEiM and TE material to ensure stable and efficient device performance. However, the behavior of ρ_c in the TE leg is very complex. During fabrication, uncontrollable reactions between TEiM and TE materials usually occur, challenging the theoretical prediction of ρ_c on the one hand. For another, ρ_c is not a constant after fabrication and usually degrades due to atomic diffusion and reaction under high temperatures over time^{25,31}. Although selecting or designing suitable TEiMs can mitigate ρ_c degradation^{6,36,38–42}, the thermodynamically driven atomic diffusion and reaction, especially at high temperatures, always challenges the achievements of long-term reliable contacts in TE legs.

MgAgSb has attracted considerable attention due to its high TE performance near room temperature^{43–49}. Initially, Ag has been used as the TEiM for fabrication of its TE leg, achieving low ρ_c and high conversion efficiency η of 8.5% in both single TE leg and two-pair TE device^{50–54}. However, a recent study has shown that ρ_c in Ag/MgAgSb increases substantially from ~ 6.1 to $1006.0 \mu\Omega \text{ cm}^2$ after 12 h of aging, challenging its long-term usage⁶. It is pointed out that Sb will diffuse from MgAgSb to Ag TEiM, causing Ag_3Sb impurity phases and cracks at the interface, which significantly contributes to the increased ρ_c in Ag/MgAgSb^{6,55}. To address the issues with Ag as TEiM, a screened semi-metal, MgCuSb, and a developed alloy, MgAgMn_{0.1}, have been respectively incorporated into MgAgSb. Both the TE junctions achieve a long-term low ρ_c and facilitate the improvement of η ^{6,56}.

Here, to prevent Sb diffusion from MgAgSb to TEiM, we have the idea to directly use Sb as the TEiM to develop Sb/MgAgSb TE junctions. In contrast to other TE junctions that typically show degraded ρ_c after aging, we demonstrate that this junction exhibits self-optimized ρ_c when exposed to 573 K, even in air. We analyze the structural evolution of the junction and find that Mg diffuses from MgAgSb into the Sb TEiM, which leads to Mg deficiency in MgAgSb, increasing carrier concentration and reducing ρ_c . Importantly, this Mg diffusion occurs only near the interface, which does not significantly affect the performance of MgAgSb away from the interface. For Sb TEiM, we reveal that it manifests decent σ , κ , low-cost, and excellent weldability. Using the 100-day air-aged Sb/MgAgSb junctions, we fabricate a two-pair Mg-based TE device, which achieves a maximum η of 8.1% and power density of 0.41 W cm^{-2} under a 294 K temperature gradient. This high output performance from long-term aged TE legs is rarely reported, highlighting their significant potential for lasting air-robust heat harvesting. The self-optimization phenomenon we discover can also inspire future designs of other junctions for long-term usage and pave the way for the long-awaited wide-scale application of TE power generation.

Results

Self-optimized ρ_c in Sb/MgAgSb/Sb with high air-resistance

Due to Sb diffusion and increased cracks at the Ag/MgAgSb junctions, a substantial increase in ρ_c has been observed⁶. Literature indicates that Sb deficiency in MgAgSb is detrimental to its performance⁴⁶. To suppress Sb diffusion from MgAgSb to the TEiM, we directly employ Sb as the TEiM in MgAgSb, forming the Sb/MgAgSb TE junction. Generally, long-term low ρ_c is significantly more desirable than merely achieving an initial low ρ_c in the junction. Therefore, the Sb/MgAgSb junction was aged at 573 K in the air for periods ranging from 7 to 30 days to investigate changes in ρ_c .

As shown in Fig. 1a, two distinct regions can be identified in the probe distance dependence of resistance, corresponding to the Sb TEiM and MgAgSb. Notably, when probing from Sb to MgAgSb, an increase in resistance can be observed. For the as-fabricated Sb/MgAgSb (0 days), a rapid initial increase in resistance is noticed at the interface, followed by a milder increase in the MgAgSb away from the interface. This rapid initial increase is attributed to the marked ρ_c between the Sb TEiM and MgAgSb. As aging progresses, the rapid initial increase in resistance near the interface diminishes, indicating a reduction in ρ_c between the Sb TEiM and MgAgSb. The inset of Fig. 1a presents a zoomed-in view of the probe distance dependence of resistance, detailing the gradual optimization of ρ_c with aging. It is noteworthy that the resistivity of MgAgSb remains unchanged, which is evidenced by the consistent slope in the MgAgSb region. The unchanged resistivity in MgAgSb also indicates its excellent stability in air.

Based on multiple measurements and averaging the ρ_c at both sides of the Sb/MgAgSb/Sb TE leg (Supplementary Figs. 1–4), ρ_c is found to decrease from $20.8 \mu\Omega \text{ cm}^2$ to $7.9 \mu\Omega \text{ cm}^2$ after 30 days of aging (Fig. 1b). It is worth noting that in contrast to the significant increase in ρ_c in Ag/MgAgSb with aging, the ρ_c of the Sb/MgAgSb junction gradually decreases over time. Although the ρ_c of Sb/MgAgSb is relatively higher compared to MgCuSb and MgAgMn_{0.1} (Supplementary Fig. 5), it is important to note that the Sb/MgAgSb junction was aged at 573 K, a higher temperature than the aging conditions used for Ag, MgAgMn_{0.1}, and MgCuSb. Moreover, unlike the vacuum environments used for Ag, MgAgMn_{0.1}, and MgCuSb^{6,50,51,53,56,57}, the Sb/MgAgSb junction was aged directly in air. The ability to withstand high air resistance at elevated temperatures allows Sb/MgAgSb to maximize the performance of MgAgSb under such challenging conditions, highlighting its strong potential for practical applications. More interestingly, this self-optimized ρ_c with aging has not been reported in previous studies, as shown in Fig. 1c, where nearly all TE junctions exhibit degraded ρ_c over time^{6,36,37,39,41,42,56–65}. The optimized ρ_c in this work suggests that the aging will not always degrade contact properties. On the contrary, if appropriate metals, alloys, or intermetallics can be identified or designed, long-term reliable contacts with low ρ_c are achievable.

Mg diffusion from MgAgSb to Sb at the junction

The self-optimized ρ_c at the interface, along with the unchanged resistivity away from it, suggests that the changes in properties in Sb/MgAgSb occur only near the interface and do not affect the properties farther away. Therefore, it is necessary to investigate how structure evolves near the interface in Sb/MgAgSb junctions over time with aging. Scanning electron microscopy (SEM) equipped with energy-dispersive spectroscopy (EDS) was employed, and Fig. 2a shows the SEM images of Sb/MgAgSb junctions after 0 days, 7 days and 30 days of aging. Line scans of Mg, Ag and Sb across the interface, shown in Fig. 2b, indicate obvious Mg diffusion from MgAgSb into Sb TEiM. Figure 2c–e display EDS mappings for Mg, Ag, and Sb, providing a clearer view of the element's evolution with aging time. Initially, a clear interface can be observed, with Sb serving as TEiM on the left and MgAgSb as TE material on the right. As aging progresses, Mg gradually

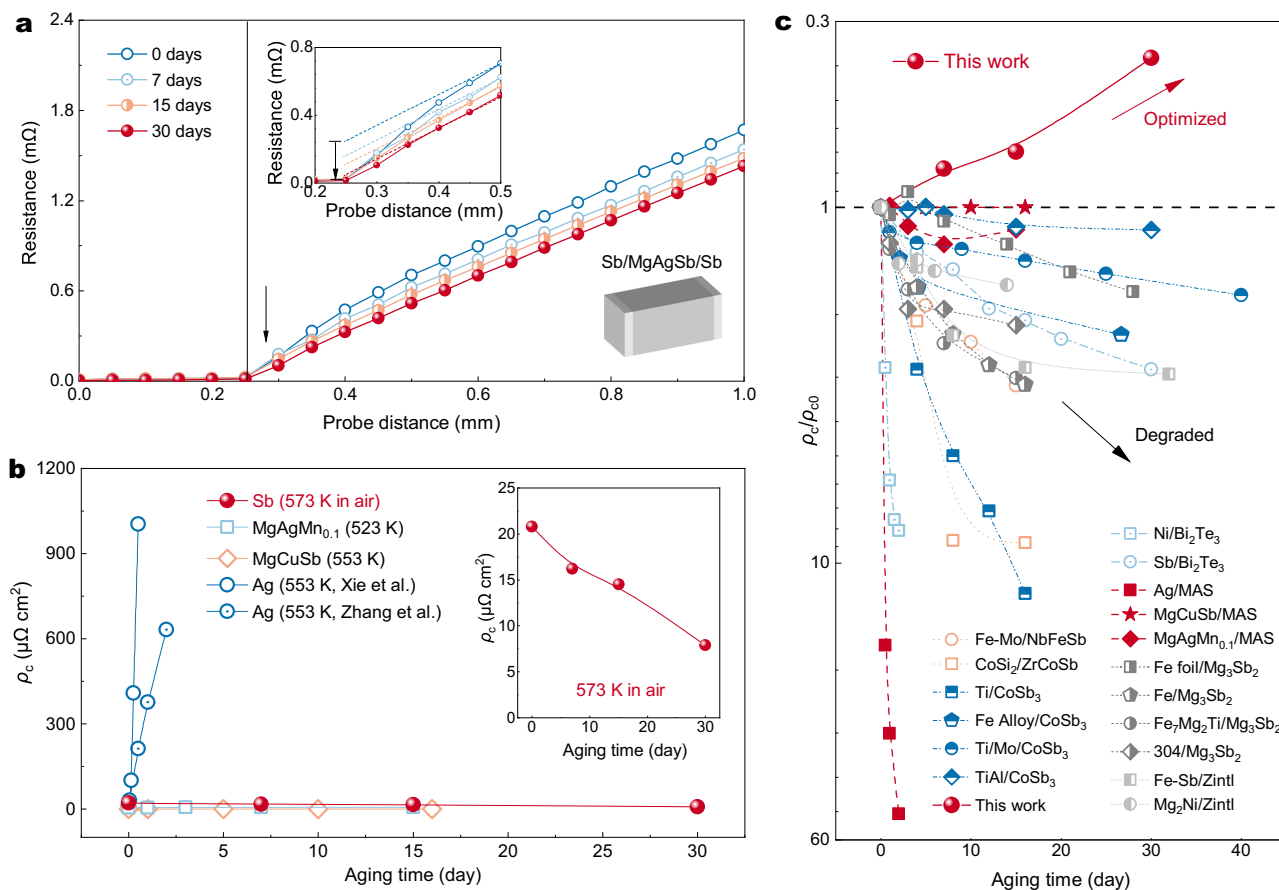


Fig. 1 | Self-optimized ρ_c in Sb/MgAgSb/Sb aged at 573 K in air. a Probe distance dependence of resistance in Sb/MgAgSb TE junctions after 0–30 days aging; **b** aging time dependence of ρ_c in Sb/MgAgSb junction compared to other MgAgSb-

based TE junctions from literature^{6,56,57}; **c** aging time dependence of ρ_c/ρ_{c0} ratio in Sb/MgAgSb and its comparison to TE junctions from literature^{6,36,37,39,41,42,56–65}, where ρ_{c0} represents the initial value of ρ_c .

diffuses from the MgAgSb into the Sb TEIM, creating a Mg-rich region about 10 μm from the original interface. While Ag shows minimal diffusion, an Sb-deficient region forms in the same Mg-rich region in the Sb TEIM. Additionally, some scattered Sb-rich phases are detected within the MgAgSb.

To further investigate the microstructure of the Sb/MgAgSb junction, an enlarged view is provided in Fig. 2f, where Mg-rich with Sb-deficient areas in the Sb TEIM, as well as scattered Sb-rich phases in the MgAgSb region are more obvious. Additionally, intensified Ag signals in the Ag mapping can be noticed within MgAgSb, suggesting the formation of Ag-rich phases. This is likely due to Mg diffusion, which leads to Mg deficiency and consequently causes Ag-rich and Sb-rich areas in MgAgSb. The overlapped mappings of Mg, Ag, and Sb in Fig. 2f offer a more comprehensive view of the phases present in the Sb/MgAgSb junction. Further semi-quantitative spot analysis was conducted to determine the specific composition at the Sb/MgAgSb junction. As shown in Supplementary Fig. 6, the composition of TEIM and TE material away from the interface is predominately Sb and MgAgSb, respectively. Near the interface, the composition of TEIM and TE material is found to be mainly Sb and MgAgSb with large amounts of Ag_3Sb , respectively (Supplementary Fig. 7). The formation of these impurities is attributed to Mg diffusion from MgAgSb to Sb, which also leads to the formation of Mg_3Sb_2 in Sb TEIM, as shown in Supplementary Fig. 8.

Historically, Ag_3Sb has been considered detrimental to the performance of MgAgSb⁶⁶, and will increase ρ_c ^{6,55}. The content of Ag_3Sb near the interface is revealed to progressively increase with aging due to continued Mg diffusion (Supplementary Fig. 9). However, in this

study, the presence of Ag_3Sb near the interface does not increase ρ_c . On the contrary, a reduction in ρ_c is observed. Notably, cracks have frequently been found at the interface besides Ag_3Sb when using Ag as TEIM⁶. However, no cracks were found at the interface in this work. Importantly, the Mg diffusion observed in the Sb/MgAgSb junction may contribute to stronger bonding between Sb and MgAgSb.

Despite the evident Mg diffusion observed in Fig. 2, a question arises as to why the diffusion of Sb toward MgAgSb and Ag toward Sb is not as pronounced, given their chemical potential differences on both sides. We propose that Mg, being chemically active and having a small atomic radius, can readily diffuse from MgAgSb to Sb, leading to the formation of Mg_3Sb_2 . Simultaneously, the resulting Mg deficiency in MgAgSb facilitates the formation of Ag_3Sb and Sb within MgAgSb. The Sb impurities formed at the MgAgSb interface may act as a barrier, inhibiting the diffusion of Sb from the Sb TEIM into MgAgSb, while the formation of Ag_3Sb at the interface may similarly restrict Ag diffusion toward Sb.

The mechanism behind reduced ρ_c

Although significant Mg diffusion from MgAgSb into Sb is observed in the Sb/MgAgSb junction, the underlying mechanism for the reduced ρ_c remains unclear. Based on the observation in Fig. 2a–f, it is evident that Mg diffusion from MgAgSb to Sb becomes significant with aging. The diffused Mg reacts with Sb to form Mg_3Sb_2 impurities, while the depletion of Mg in MgAgSb leads to the decomposition of MgAgSb into Ag_3Sb and Sb. Figure 3a provides a schematic diagram illustrating the structural changes with aging. To investigate whether Mg diffusion plays a key role in reducing ρ_c , we deliberately reduced the Mg content

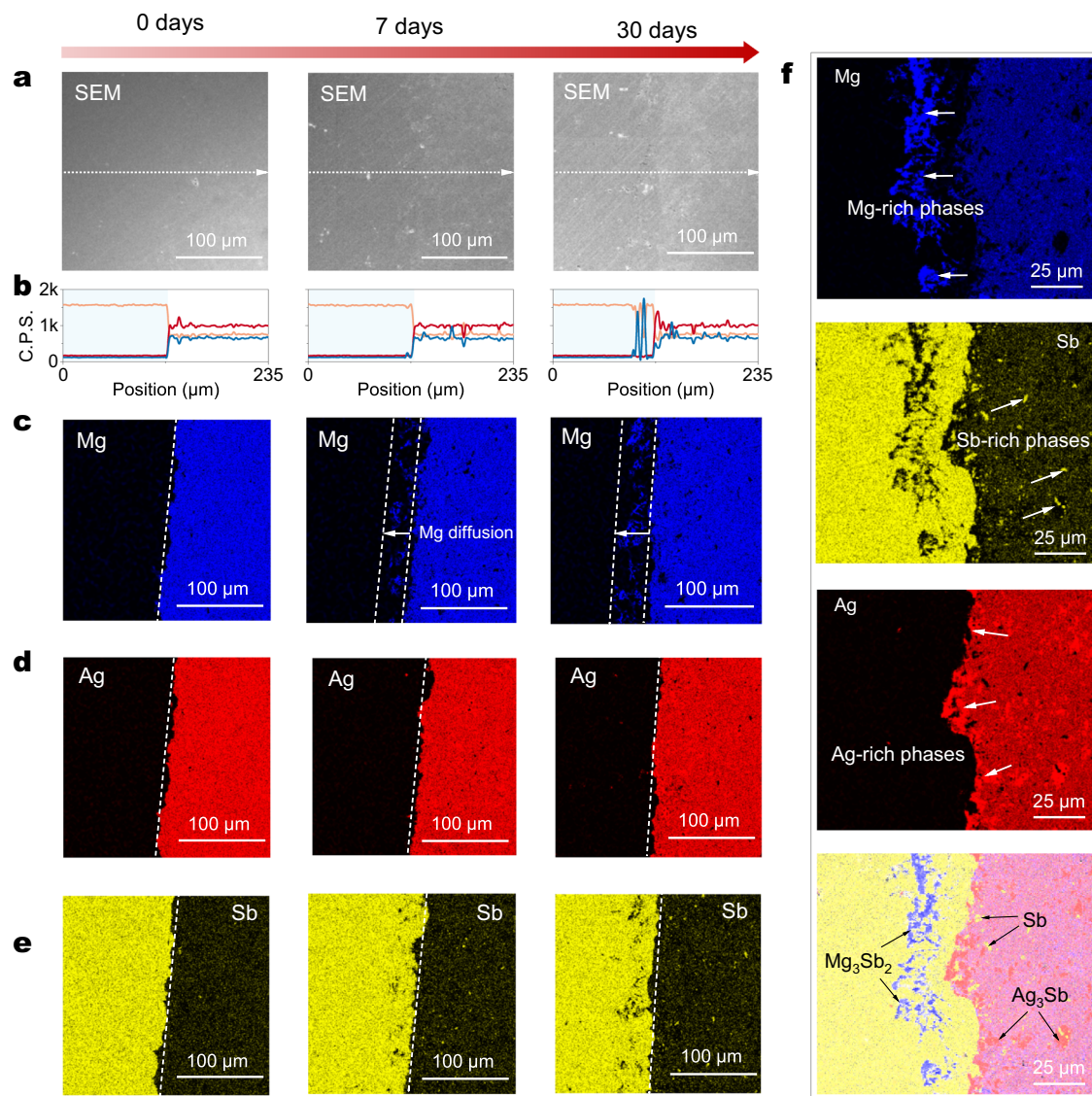


Fig. 2 | Structural analysis of Sb/MgAgSb junction. **a** SEM images, **b** line scan of Mg, Ag, and Sb, and elemental mappings of **c** Mg, **d** Ag, and **e** Sb in Sb/MgAgSb junction after 0 days, 7 days, and 30 days of aging; **f** enlarged view of elemental mappings of Mg, Ag, Sb, and overlapped Mg, Ag, Sb in Sb/MgAgSb junction after 30 days of aging.

in MgAgSb to simulate this Mg diffusion and synthesized Mg-deficient $\text{Mg}_{1-x}\text{AgSb}$ ($x = 0.05$ and 0.1). The X-ray diffraction (XRD) patterns of these Mg-deficient samples, shown in Fig. 3b, reveal impurity phases of Ag_3Sb and Sb, consistent with the EDS analysis. Using these Mg-deficient samples, we fabricated Sb/ $\text{Mg}_{1-x}\text{AgSb}$ junctions to examine changes in ρ_c . As shown in Fig. 3c, the ρ_c is indeed reduced with decreasing Mg content in $\text{Mg}_{1-x}\text{AgSb}$, confirming Mg deficiency plays a crucial role in lowering ρ_c .

Considering that Mg_3Sb_2 forms in Sb TEIM at a distance from the interface, the contact between Sb and MgAgSb gradually evolves into the contact between Sb and MgAgSb with Ag_3Sb . Based on their density of states (DOS) near Fermi level E_F (Fig. 3d), it can be found that MgAgSb is a semiconductor, Ag_3Sb is a typical metal, and Sb is a semimetal. Typically, there are no energy barriers at the junction between a metal and a semimetal, which means the increased presence of Ag_3Sb metallic phases at the interface may help reduce ρ_c . Moreover, according to metal-semiconductor contact theory, ρ_c depends on both the barrier height (ϕ_B) and carrier concentration n , with the relationship simplified as $\rho_c \sim \exp(q\phi_B/n^{1/2})$, where q is the elemental charge^{29,33,67}. Therefore, increasing n can help reduce ρ_c ^{68,69}. Figure 3e, f demonstrates that, as the Mg content decreases, S of $\text{Mg}_{1-x}\text{AgSb}$

decreases, while σ increases, indicating that n increases with reduced Mg content. This suggests that Mg deficiency not only results in the formation of Ag_3Sb and Sb impurities but also significantly enhances n in $\text{Mg}_{1-x}\text{AgSb}$. Similarly, in the Sb/MgAgSb junction, Mg diffusion from MgAgSb to Sb promotes the formation of the metallic Ag_3Sb phase and enhances n at the interface, thereby contributing to the reduction in ρ_c .

Intrinsically, n influences the electron transport mechanism across the interface. In a metal/p-type semiconductor contact, a Schottky barrier ϕ_B forms when the work function of the metal (ϕ_m) is lower than that of the semiconductor (ϕ_s), as shown in Fig. 3g. For Sb/MgAgSb, such a barrier is formed due to the work functions of Sb (4.40 eV) and MgAgSb (4.56 eV)^{4,6}. Typically, electron transport across the interface follows thermionic emission when the n of the material is low or moderate. If n increases, E_{FS} will approach the valence band edge (E_{VS}) of the semiconductor, which will make the width of the depletion layer W narrower (Fig. 3h). At this point, electron tunneling effects become more significant, allowing for a much higher current and lowering ρ_c . Notably, in this study, Mg thermodynamically diffuses from MgAgSb into the Sb TEIM, naturally forming a layer with high n at the interface. This high n layer directly bonds to the Sb TEIM, which

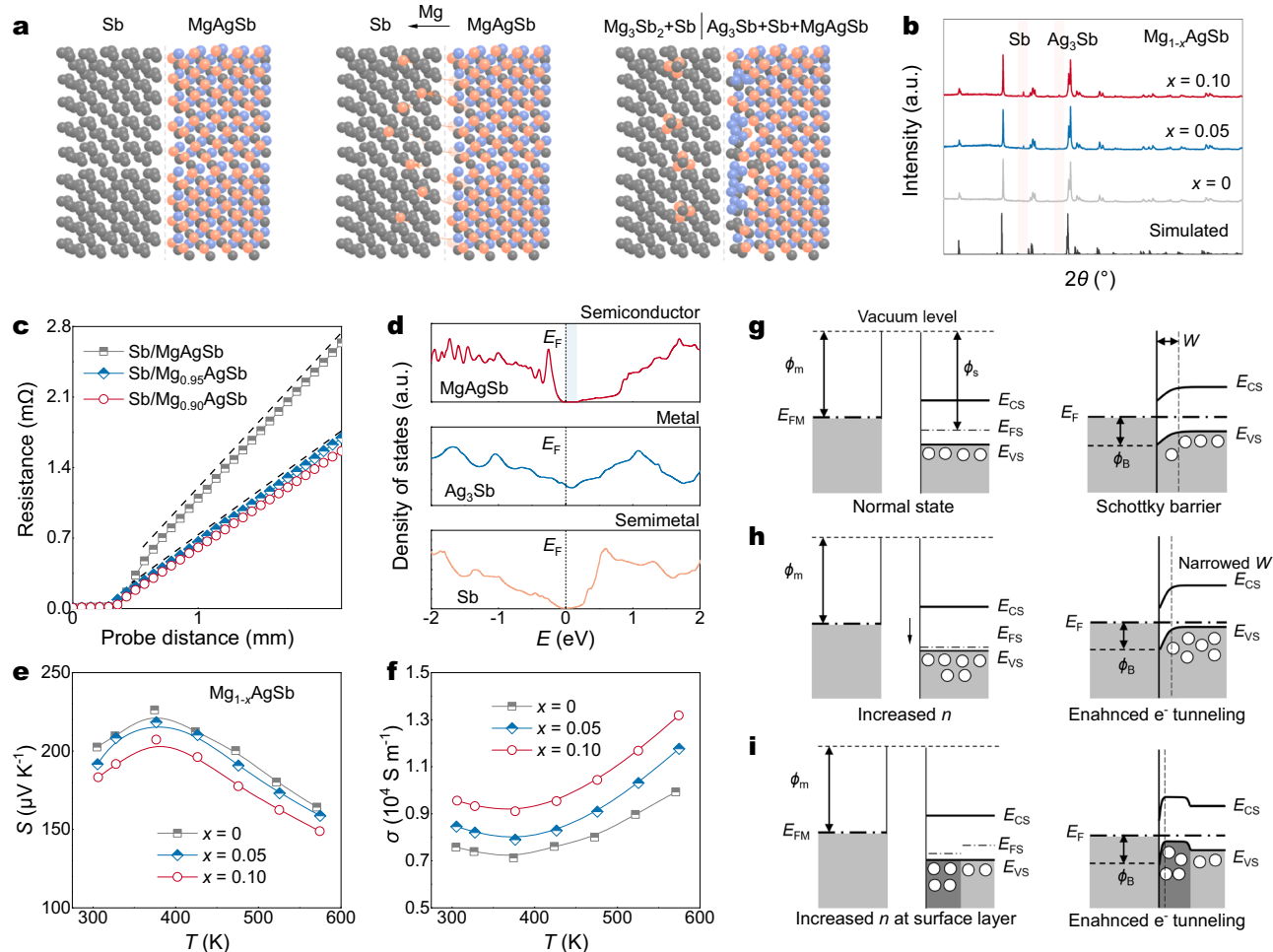


Fig. 3 | Reduced ρ_c from increased carrier concentration for enhanced electron tunneling. **a** Schematic diagram of structural changes in Sb/MgAgSb with aging; **b** XRD patterns of $\text{Mg}_{1-x}\text{AgSb}$ and **c** probe distance dependence of resistance in Sb/ $\text{Mg}_{1-x}\text{AgSb}$ TE junctions; **d** DOS of MgAgSb, Ag_3Sb and Sb; temperature dependence

of S and σ of $\text{Mg}_{1-x}\text{AgSb}$; energy band diagram of the contact between metal and **g** normal p-type semiconductor, **h** p-type semiconductor with increased n and **i** p-type semiconductor with a high n layer, specifically for the diagram in Sb/ MgAgSb after aging.

reduces the W of the depletion layer and promotes electron tunneling. The schematic diagram in Sb/MgAgSb after aging is illustrated in Fig. 3i.

However, despite the ρ_c being reduced, there are concerns about the alerted performance of MgAgSb near the interface. In Sb/MgAgSb junction, it is noteworthy that the overall composition of MgAgSb away from the interface does not significantly change after 30 days of aging, as shown in Supplementary Fig. 10. Consequently, the performance of MgAgSb away from the interface remains largely unchanged, as evidenced by the consistent Seebeck coefficient in both the Sb/MgAgSb/Sb junction and the MgAgSb material at different aging times (Supplementary Fig. 11). Thus, the Mg diffusion in Sb/MgAgSb only forms a thin high- n layer, just micrometers thick near the interface, which helps reduce ρ_c when in contact with Sb. Heavily doping the surface layer of a semiconductor is a common strategy in semiconductor devices to reduce the barrier width and facilitate ohmic contacts between the metal and semiconductor. This approach may be effective for achieving low ρ_c in TE junctions in the future.

Efficient η of Sb/MgAgSb-based TE device

Typically, high σ and κ are desired for the TEiM to minimize energy loss during heat and electricity transport. Here, we compare Sb TEiM with other TEiMs used in MgAgSb. As shown in Fig. 4a, b, Sb exhibits moderate values of both σ and κ compared to Ag, MgAgMn_{0.1}, and

MgCuSb^{6,56,70}. Based on the σ , κ , S (as shown in Supplementary Fig. 12) of these TEiMs, we simulated the maximum conversion efficiency η_{\max} and maximum power P_{\max} of a single MgAgSb TE leg. The TEiM was assumed to have a height of 0.5 mm at both ends of the leg without considering ρ_c . As shown in Supplementary Fig. 13, despite large differences in σ and κ , the variation in η_{\max} and P_{\max} of these single TE legs are relatively small. For MgCuSb sintered at 573 K, which has lower σ and κ , it demonstrates correspondingly lower η_{\max} and P_{\max} . Since power output is accumulated across multiple legs in a TE device, which usually consists of 30 or more TE legs, high σ and κ are always desirable. But if the TEiM layer is made thinner, its impact on η_{\max} and P_{\max} will diminish.

Cost is another factor that could be considered, especially with potential large-scale applications. Figure 4c shows that Sb and MgCuSb are much more cost-effective than Ag and MgAgMn_{0.1}⁷¹. In addition, weldability is an important aspect of the TEiM that should be considered. A key function of TEiMs is to facilitate the joining of TE legs with electrodes. Without proper weldability, additional layers are often required for the joining, which complicates the fabrication process. Compared to MgAgMn_{0.1} and MgCuSb, Sb demonstrates excellent weldability. The inset in Fig. 4d shows that conventional Sn-based solder can easily wet the surface of Sb. Moreover, as shown in Fig. 4d, the joint between Sb/MgAgSb and Cu electrode made with this solder exhibits very low ρ_c , further highlighting the advantages of using Sb as a promising TEiM for future practical applications.

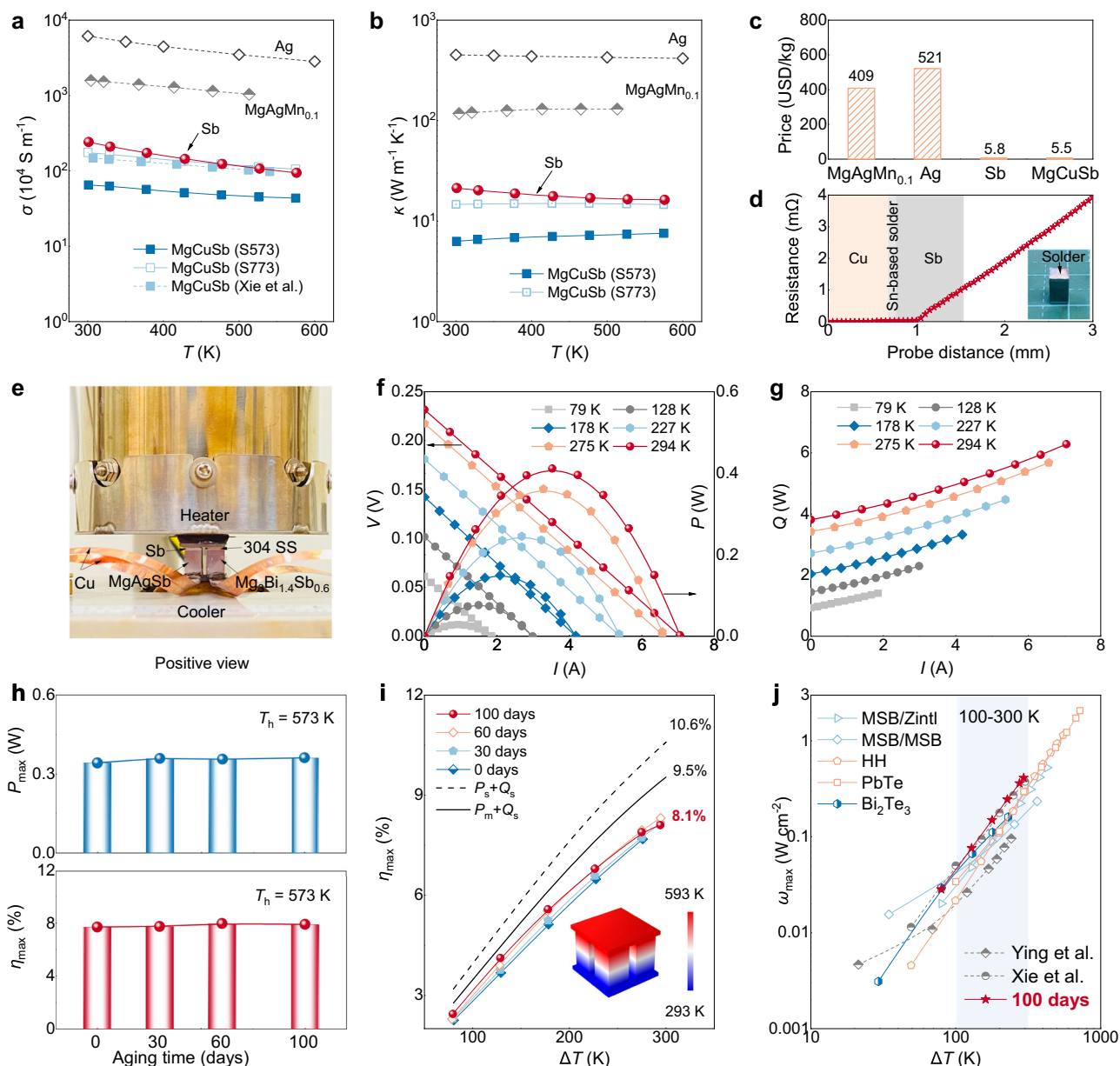


Fig. 4 | Conversion efficiency two-pair TE device based on Sb/MgAgSb TE junction. *T* dependence of **a** σ , **b** κ and **c** price of Sb and other TEIMs in MgAgSb, where σ of Ag, MgAgMn_{0.1} are sourced from literature^{6,56,70}, while κ of Ag and MgAgMn_{0.1} are calculated based Wiedemann-Franz law; **d** probe distance dependence of resistance for the joint between Sb/MgAgSb and Cu electrode made with Sn-based solder, with an optical image of the Sb/MgAgSb/Sb leg wetted by Sn-based solder included in the inset; **e** optical image of two-pair TE device and the measurement set-up; **f** V and P , and **g** Q under different ΔT s of the

two-pair TE device based on Sb/MgAgSb/Sb legs after 100 days of aging in air; **h** aging time dependence of P_{\max} and η_{\max} when T_h is 573 K; **i** ΔT dependence of η_{\max} in MgAgSb/Mg₃Sb_{0.6}Bi_{1.4} two-pair TE devices, where P_m , P_s and Q_s represent measured power, simulated power and simulated heat flow, respectively; **j** ΔT dependence of ω_{\max} in MgAgSb/Mg₃Sb_{0.6}Bi_{1.4} two-pair TE device and its comparison with other two-pair TE devices in the literature^{6,42,51,56,73–75}, where the abbreviations MSB, HH and BST refer to Mg₃(Sb,Bi)₂, half-Heusler and (Bi,Sb)₂Te₃, respectively.

To further validate the reliability of the Sb/MgAgSb TE junctions developed in this study, two-pair Mg-based TE devices are fabricated, with the schematic diagram of the module's dimensions shown in Supplementary Fig. 14. The n-type legs were made of Mg₃Sb_{0.6}Bi_{1.4}, with their TE performance detailed in Supplementary Fig. 15. The as-fabricated Sb/MgAgSb/Sb TE legs without aging were used for initial testing. Optical images of the measurement set-up and the two-pair TE device are shown in Fig. 4e. Supplementary Fig. 16 shows the voltage (V), power output (P), heat flow (Q), and conversion efficiency (η) of the device under varying ΔT and applied current (I), where η_{\max} reaches approximately 7.7% at a ΔT of 276 K. After aging Sb/MgAgSb/Sb legs at 573 K in air for 30 and 60 days, they are coupled with n-type

Mg₃Sb_{0.6}Bi_{1.4} to make another two two-pair TE devices. Measurements in Supplementary Figs. 17–18 show that η_{\max} of them reach 7.9% at ΔT ~ 275 K. Furthermore, Sb/MgAgSb/Sb legs were aged at 573 K in the air for an additional 40 days (totaling 100 days). I -dependent V , P and Q under different ΔT s measured in its corresponding two-pair TE device is shown in Fig. 4f, g. It reveals that η_{\max} can reach 8.1% under ΔT ~ 294 K. While this value is slightly lower than the state-of-the-art Ag, MgCuSb, and MgAgMn_{0.1} used as TEIMs in MgAgSb^{6,54,56}, several factors should be considered. Excluding variations in measurement conditions and potential errors across different measurement systems, the shorter height of the TE legs in this study compared to those in the literature^{6,54,56} likely reduces efficiency but enhances power

generation, contributing to the impressive high P_{\max} of 0.41 W achieved in this work. More importantly, the maintained P_{\max} and η_{\max} in these two-pair TE devices based on Sb/MgAgSb after 0, 30 days, 60 days, and 100 days of air-aging sufficiently confirms the long-term reliable contacts in Sb/MgAgSb, as well as emphasizing the excellent stability of MgAgSb despite some Mg diffusion at the interface (Fig. 4h).

To explore further potential improvements, a simulation is conducted to evaluate the performance of the two-pair TE device, taking into account the TE performance of MgAgSb and $\text{Mg}_{3.2}\text{In}_{0.02}\text{Sb}_{0.595}\text{Bi}_{1.4}\text{Te}_{0.005}$, ρ_c of both n-type and p-type legs, as well as the properties of the TEIMs. The inset in Fig. 4i presents the simulated two-pair TE device under a hot side temperature of 593 K and a cold side temperature of 293 K. The simulation results indicate that the η_{\max} could reach 10.6%. Detailed simulated I -dependent of V , P , Q , and η is shown in Supplementary Fig. 19. Generally, the measured P tends to be lower, while the measured Q tends to be higher than the simulated results. In practical measurements, P can usually be accurately assessed, but precisely measuring Q is often challenging⁷². To better illustrate the potential of the developed two-pair TE device, the simulated heat flow Q_s and measured power output P_m were used to calculate η_{\max} . When ΔT is 300 K, the two-pair TE device can demonstrate η_{\max} of 9.5%.

Supplementary Fig. 20 displays the discrepancies in open-circuit voltage V_o , internal resistance R , heat flow without current Q_o , and P_{\max} between the measurements and simulations, indicating potential room for further improvement of the developed two-pair TE device. In fact, the achieved maximum power density ω_{\max} of 0.41 W cm⁻² and η_{\max} of 8.1% in our present MgAgSb/ $\text{Mg}_{3.2}\text{In}_{0.02}\text{Sb}_{0.595}\text{Bi}_{1.4}\text{Te}_{0.005}$ -based TE device is also highly impressive when compared to other two-pair TE devices under similar temperature gradients^{6,42,51,56,73–75}, especially in the 100–300 K range (Fig. 4j and Supplementary Fig. 21). Furthermore, a distinguishing feature of Sb/MgAgSb/Sb is its exceptional durability. The junction remains stable even after 100 days of aging in air, a characteristic rarely reported in the literature for other TE materials. This highlights its strong potential for long-term applications.

Discussion

In summary, we report for the first time a self-optimized contact resistivity ρ_c in Sb/MgAgSb TE junctions. Dramatically different from conventional TE junctions that typically experience increased resistivity after high-temperature aging, ρ_c of Sb/MgAgSb junction gradually optimized when exposed to 573 K, even in air. Mg diffusion from MgAgSb into the Sb TEIM is revealed, which leads to Mg deficiency in MgAgSb, resulting in increased carrier concentration n . This increased n enhances electron tunneling between MgAgSb and the Sb TEIM, effectively reducing ρ_c . The Mg diffusion is revealed to occur near the interface, which does not affect the performance of the main bulk MgAgSb material. For Sb TEIM, it is revealed to possess decent σ , κ , low-cost, and excellent weldability, which allows for its direct bonding to electrodes without the need for additional layers. The practical application of our developed TE junction is highlighted by the fabrication of a two-pair Mg-based TE device, which achieves ω_{\max} of 0.41 W cm⁻² and η_{\max} of 8.1% under a 294 K temperature difference, even after Sb/MgAgSb/Sb TE legs were aged at 573 K in air for 100 days. This finding underscores the significant potential of the developed Sb/MgAgSb junctions for long-term efficient low-grade heat harvesting. Additionally, the self-optimization phenomenon observed in this study offers valuable insights that could inspire the design of future TE junctions aimed at long-term applications, and thereby paving the way for the long-awaited wide-scale application of TE power generation.

Methods

Materials synthesis

$\text{Mg}_{1-x}\text{Ag}_{0.97}\text{Sb}_{0.99}$ with 0.625 wt% $\text{C}_{18}\text{H}_{36}\text{O}_2$ ($x = 0, 0.05, 1$) (denoted as $\text{Mg}_{1-x}\text{AgSb}$ in the main text and below), MgCuSb and

$\text{Mg}_{3.2}\text{In}_{0.02}\text{Sb}_{0.595}\text{Bi}_{1.4}\text{Te}_{0.005}$ (denoted as $\text{Mg}_3\text{Sb}_{0.6}\text{Bi}_{1.4}$ in the main text and below) were synthesized by using Mg turnings (99.95%), Ag powers (99.99%) Sb shots (99.999%), Cu powder (99.999%), Bi shots (99.999%), Te shots (99.999%) and In powders (99.99%). The raw materials were weighted stoichiometrically and then put into the ball-milling jar with the inside of argon. Then, the jars were mechanically alloyed for 5 h, 20 h, and 5 h for $\text{Mg}_{1-x}\text{AgSb}$, MgCuSb and $\text{Mg}_{3.2}\text{In}_{0.02}\text{Sb}_{0.595}\text{Bi}_{1.4}\text{Te}_{0.005}$, respectively (SPEX-8000D). The obtained powders from the jars were then consolidated into the bulk by vacuum spark plasma sintering. $\text{Mg}_{1-x}\text{AgSb}$ was sintered under 573 K and 60 MPa for 5 min (SPS-322Lx, Dr. Sintering). MgCuSb was sintered under 573 K or 773 K and 60 MPa for 5 min (SPS-322Lx, Dr. Sintering). $\text{Mg}_{3.2}\text{In}_{0.02}\text{Sb}_{0.595}\text{Bi}_{1.4}\text{Te}_{0.005}$ was sintered under 973 K and 60 MPa for 10 min (SPS-1080 System, SPS SYNTEx INC).

Characterization and measurements

X-ray diffractometer (SmartLab3, Rigaku) with $\text{Cu K}\alpha$ radiation (40 kV and 15 mA) was used to characterize the phases of the obtained $\text{Mg}_{1-x}\text{AgSb}$ samples. ZEM-3 (Advance Riko) was employed to measure electrical transport properties (S and σ) of the samples, which have an uncertainty of $\pm 5\%$. LFA467 (Netzsch) was used to determine the thermal diffusivity D of the samples, with an uncertainty of $\pm 3\%$. The κ was calculated using the formula $\kappa = D\rho C_p$, where ρ and C_p represent the density and heat capacity of the samples, obtained by the Archimedes method and the Dulong-Petit law, respectively. The figure of merit zT was calculated based on above S , σ and κ using the equation $zT = S^2\sigma T/\kappa$.

TE junction fabrication and characterization

Sb/MgAgSb/Sb leg was fabricated by sandwiching two layers of Sb as the interface material and then sintered by SPS under 573 K and 60 MPa for 5 min. The obtained Sb/MgAgSb/Sb were cut into dice with dimensions of $3.8 \times 3.8 \times 6$ mm³. Sb/MgAgSb TE junctions were aged at 573 K in the air for 0, 7, 15, and 30 days for characterization and contact resistivity measurements. The contact resistance of the Sb/MgAgSb TE junctions was measured by a 2-axis resistance distribution measurement instrument (SI331, Mottainai energy). The composition distribution of these TE junctions was investigated by using scanning electron microscopy (FESEM, Hitachi SU8000) equipped with an energy dispersive spectrometer (EDS, XFlash FlatQUAD 5060 F).

TE device fabrication, measurement, and simulation

Two-pair TE device was assembled using p-type MgAgSb and n-type $\text{Mg}_3\text{Sb}_{0.6}\text{Bi}_{1.4}$ TE legs. Sb and 304 stainless steel were used as TEIMs for MgAgSb and $\text{Mg}_3\text{Sb}_{0.6}\text{Bi}_{1.4}$, respectively. Mini-PEM (Advance Riko) was used to measure the output power and conversion efficiency the two-pair TE device. The measurement was conducted under vacuum conditions. The temperature gradient was established by maintaining the cold-side temperature at 293 K, while the hot-side temperatures varied from 373 K to 593 K. The finite-element simulations were performed with COMSOL Multiphysics® software to simulate the conversion efficiency and power of the TE leg with different TEIM and the two-pair TE device, the thermal contact resistance between the multiple interfaces of the TE device was not considered in this work.

First-principles calculations

First-principles calculations were performed to calculate the density of states (DOS) of MgAgSb, Ag_3Sb and Sb. These calculations were conducted using software Vienna ab initio Simulation Package (VASP) with the projector augmented-wave method^{76,77}. Here, the generalized gradient approximation with the Perdew-Burke-Ernzerhof functional GGA-PBE and modified Becke-Johnson (mBJ) were used as exchange-correlation functionals to achieve a more accurate estimation of the bandgap^{78,79}. 500 eV was used as plane-wave energy cutoff. The convergence criteria for Hellmann–Feynman

force on each atom energy and total energy were set to $0.001 \text{ eV } \text{\AA}^{-1}$ and 10^{-8} eV , respectively. Geometry relaxation was first performed using Gamma-centered k -point sampling with $k = 30/L$, where L is the lattice parameter of crystal. The relaxed structure was then used for self-consistent static calculations with $k = 60/L$. VASP⁸⁰ has been used to post-process the calculated data for obtaining the DOS of MgAgSb, Ag₃Sb and Sb.

Data availability

All data generated or analyzed during this study are included in this published article (and its supplementary information file).

References

- Cohen, S. S. & Gildenblat, G. S. *Metal-semiconductor contacts and devices* (Academic Press, 1986).
- Liu, Y. et al. Approaching the Schottky–Mott limit in van der Waals metal–semiconductor junctions. *Nature* **557**, 696–700 (2018).
- Kwon, G. et al. Interaction- and defect-free van der Waals contacts between metals and two-dimensional semiconductors. *Nat. Electron.* **5**, 241–247 (2022).
- Shen, P.-C. et al. Ultralow contact resistance between semimetal and monolayer semiconductors. *Nature* **593**, 211–217 (2021).
- Jiang, J. et al. Yttrium-doping-induced metallization of molybdenum disulfide for ohmic contacts in two-dimensional transistors. *Nat. Electron.* **7**, 545–556 (2024).
- Xie, L. et al. Screening strategy for developing thermoelectric interface materials. *Science* **382**, 921–928 (2023).
- He, J. & Tritt, T. M. Advances in thermoelectric materials research: looking back and moving forward. *Science* **357**, eaak9997 (2017).
- Snyder, G. J. & Toberer, E. S. Complex thermoelectric materials. *Nat. Mater.* **7**, 105–114 (2008).
- Petsagkourakis, I. et al. Thermoelectric materials and applications for energy harvesting power generation. *Sci. Technol. Adv. Mater.* **19**, 836–862 (2018).
- He, R., Schierning, G. & Nielsch, K. Thermoelectric devices: a review of devices, architectures, and contact optimization. *Adv. Mater. Technol.* **3**, 1700256 (2018).
- Hendricks, T., Caillat, T. & Mori, T. Keynote review of latest advances in thermoelectric generation materials, devices, and technologies 2022. *Energies* **15**, 7307 (2022).
- Zhu, T. et al. Compromise and synergy in high-efficiency thermoelectric materials. *Adv. Mater.* **29**, 1605884 (2017).
- Mori, T. Novel principles and nanostructuring methods for enhanced thermoelectrics. *Small* **13**, 1702013 (2017).
- Shi, X.-L., Zou, J. & Chen, Z.-G. Advanced thermoelectric design: from materials and structures to devices. *Chem. Rev.* **120**, 7399–7515 (2020).
- Yang, Q. et al. Flexible thermoelectrics based on ductile semiconductors. *Science* **377**, 854–858 (2022).
- Qin, Y. et al. Grid-plainification enables medium-temperature PbSe thermoelectrics to cool better than Bi₂Te₃. *Science* **383**, 1204–1209 (2024).
- Li, A. et al. High performance magnesium-based plastic semiconductors for flexible thermoelectrics. *Nat. Commun.* **15**, 5108 (2024).
- Wang, L. et al. High-performance Mg₃Sb₂-based thermoelectrics with reduced structural disorder and microstructure evolution. *Nat. Commun.* **15**, 6800 (2024).
- Bano, S., Chetty, R., Babu, J. & Mori, T. Mg₃(Sb,Bi)₂-based materials and devices rivaling bismuth telluride for thermoelectric power generation and cooling. *Device* **2**, 100408 (2024).
- Qiu, P. et al. Suppression of atom motion and metal deposition in mixed ionic electronic conductors. *Nat. Commun.* **9**, 2910 (2018).
- Li, A., Fu, C., Zhao, X. & Zhu, T. High-performance Mg₃Sb_{2-x}Bi_x thermoelectrics: progress and perspective. *Research* **2020**, 1934848 (2020).
- Li, A. et al. Chemical stability and degradation mechanism of Mg₃Sb_{2-x}Bi_x thermoelectrics towards room-temperature applications. *Acta Mater.* **239**, 118301 (2022).
- Hu, H. et al. Highly stabilized and efficient thermoelectric copper selenide. *Nat. Mater.* **23**, 527–534 (2024).
- Liao, C.-N., Lee, C.-H. & Chen, W.-J. Effect of interfacial compound formation on contact resistivity of soldered junctions between Bismuth Telluride-Based thermoelements and copper. *Electrochem. Solid-State Lett.* **10**, P23 (2007).
- Zhao, D., Li, X., He, L., Jiang, W. & Chen, L. Interfacial evolution behavior and reliability evaluation of CoSb₃/Ti/Mo–Cu thermoelectric joints during accelerated thermal aging. *J. Alloys Compd.* **477**, 425–431 (2009).
- Zhao, D., Geng, H. & Teng, X. Fabrication and reliability evaluation of CoSb₃/W–Cu thermoelectric element. *J. Alloys Compd.* **517**, 198–203 (2012).
- Liu, W. et al. Understanding of the contact of nanostructured thermoelectric n-type Bi₂Te_{2.7}Se_{0.3} legs for power generation applications. *J. Mater. Chem. A* **1**, 13093–13100 (2013).
- Li, C. C. et al. Interfacial reactions between PbTe-based thermoelectric materials and Cu and Ag bonding materials. *J. Mater. Chem. C* **3**, 10590–10596 (2015).
- Liu, W., Jie, Q., Kim, H. S. & Ren, Z. Current progress and future challenges in thermoelectric power generation: From materials to devices. *Acta Mater.* **87**, 357–376 (2015).
- Chen, S.-w. et al. Interfacial reactions in the Ni/(Bi_{0.25}Sb_{0.75})₂Te₃ and Ni/Bi₂(Te_{0.9}Se_{0.1})₃ couples. *J. Alloys Compd.* **686**, 847–853 (2016).
- Shen, J. et al. Low contact resistivity and interfacial behavior of p-Type NbFeSb/Mo thermoelectric junction. *ACS Appl. Mater. Interfaces* **11**, 14182–14190 (2019).
- Lan, Y. C., Wang, D. Z., Chen, G. & Ren, Z. F. Diffusion of nickel and tin in p-type (Bi,Sb)₂Te₃ and n-type Bi₂(Te,Se)₃ thermoelectric materials. *Appl. Phys. Lett.* **92**, 101910 (2008).
- Liu, W. & Bai, S. Thermoelectric interface materials: a perspective to the challenge of thermoelectric power generation module. *J. Materiomics* **5**, 321–336 (2019).
- Shen, L. et al. Optimization of interface materials between Bi₂Te₃-Based Films and Cu electrodes enables a high performance thin-film thermoelectric cooler. *ACS Appl. Mater. Interfaces* **14**, 21106–21115 (2022).
- Anatychuk, L. I. & Luste, O. J. Physical principles of micro-miniaturization in thermoelectricity. In: *Fifteenth International Conference on Thermoelectrics. Proceedings ICT '96*, 279–287 (IEEE, Pasadena, CA, USA, 1996).
- Wang, Z. et al. Mo-Fe/NbFeSb thermoelectric junctions: anti-thermal aging interface and low contact resistivity. *ACS Appl. Mater. Interfaces* **13**, 7317–7323 (2021).
- Xiong, B. et al. Low interfacial resistivity in CoSi₂/ZrCoSb thermoelectric junctions. *Mater. Today Energy* **25**, 100960 (2022).
- Gupta, R. P. et al. Low resistance ohmic contacts to Bi₂Te₃ using Ni and Co metallization. *J. Electrochem. Soc.* **157**, H666 (2010).
- Yin, L. et al. Reliable N-type Mg_{3.2}Sb_{1.5}Bi_{0.49}Te_{0.01}/304 stainless steel junction for thermoelectric applications. *Acta Mater.* **198**, 25–34 (2020).
- Chu, J. et al. Electrode interface optimization advances conversion efficiency and stability of thermoelectric devices. *Nat. Commun.* **11**, 2723 (2020).
- Wu, X. et al. A general design strategy for thermoelectric interface materials in n-type Mg₃Sb_{1.5}Bi_{0.5} single leg used in TEGs. *Acta Mater.* **226**, 117616 (2022).

42. Yin, L. et al. CALPHAD accelerated design of advanced full-Zintl thermoelectric device. *Nat. Commun.* **15**, 1468 (2024).
43. Kirkham, M. J. et al. Ab initio determination of crystal structures of the thermoelectric material MgAgSb. *Phys. Rev. B* **85**, 144120 (2012).
44. Zhao, H. et al. High thermoelectric performance of MgAgSb-based materials. *Nano Energy* **7**, 97–103 (2014).
45. Ying, P. et al. High performance α -MgAgSb thermoelectric materials for low temperature power generation. *Chem. Mater.* **27**, 909–913 (2015).
46. Duparchy, A. et al. Establishing synthesis–composition–property relationships for enhanced and reproducible thermoelectric properties of MgAgSb. *J. Mater. Chem. A* **10**, 21716–21726 (2022).
47. Xie, L. et al. Highly efficient thermoelectric cooling performance of ultrafine-grained and nanoporous materials. *Mater. Today* **65**, 5–13 (2023).
48. Huang, Y. et al. Intrinsically high thermoelectric performance in near-room-temperature α -MgAgSb materials. *Acta Mater.* **249**, 118847 (2023).
49. Li, A., Wang, L., Li, J. & Mori, T. Global softening to manipulate sound velocity for reliable high-performance MgAgSb thermoelectrics. *Energy Environ. Sci.* **17**, 8810–8819 (2024).
50. Kraemer, D. et al. High thermoelectric conversion efficiency of MgAgSb-based material with hot-pressed contacts. *Energy Environ. Sci.* **8**, 1299–1308 (2015).
51. Ying, P. et al. Towards tellurium-free thermoelectric modules for power generation from low-grade heat. *Nat. Commun.* **12**, 1121 (2021).
52. Liu, Z. et al. Demonstration of ultrahigh thermoelectric efficiency of $\sim 7.3\%$ in $\text{Mg}_3\text{Sb}_2/\text{MgAgSb}$ module for low-temperature energy harvesting. *Joule* **5**, 1196–1208 (2021).
53. Liu, Z. et al. Maximizing the performance of n-type Mg_3Bi_2 based materials for room-temperature power generation and thermoelectric cooling. *Nat. Commun.* **13**, 1120 (2022).
54. Ying, P. et al. A robust thermoelectric module based on MgAgSb/ $\text{Mg}_3(\text{Sb},\text{Bi})_2$ with a conversion efficiency of 8.5% and a maximum cooling of 72 K. *Energy Environ. Sci.* **15**, 2557–2566 (2022).
55. Ying, P. et al. Performance degradation and protective effects of atomic layer deposition for Mg-based thermoelectric modules. *Adv. Funct. Mater.* **34**, 2406473 (2024).
56. Wu, X. et al. A high performance eco-friendly MgAgSb-based thermoelectric power generation device near phase transition temperatures. *Energy Environ. Sci.* **17**, 2879–2887 (2024).
57. Zhang, X. et al. High cooling and power generation performance of α -MgAgSb with intrinsic low lattice thermal conductivity. *Mater. Today Phys.* **44**, 101451 (2024).
58. Li, F., Huang, X., Jiang, W. & Chen, L. Microstructure and contact resistivity of $(\text{Bi}, \text{Sb})_2\text{Te}_3/\text{Sb}$ interface. *AIP Conf. Proc.* **1449**, 458–462 (2012).
59. Gu, M., Xia, X., Li, X., Huang, X. & Chen, L. Microstructural evolution of the interfacial layer in the $\text{Ti-Al/Yb}_{0.6}\text{Co}_4\text{Sb}_{12}$ thermoelectric joints at high temperature. *J. Alloys Compd.* **610**, 665–670 (2014).
60. Gu, M. et al. Study on the high temperature interfacial stability of $\text{Ti}/\text{Mo/Yb}_{0.3}\text{Co}_4\text{Sb}_{12}$ thermoelectric joints. *Appl. Sci.* **7**, 952 (2017).
61. Sun, Z., Chen, X., Zhang, J., Geng, H. & Zhang, L. X. Achieving reliable CoSb_3 based thermoelectric joints with low contact resistivity using a high-entropy alloy diffusion barrier layer. *J. Mater. Chem.* **8**, 882–892 (2022).
62. Sun, Y. et al. Low contact resistivity and excellent thermal stability of p-type $\text{YbMg}_{0.8}\text{Zn}_{1.2}\text{Sb}_2/\text{Fe-Sb}$ junction for thermoelectric applications. *Acta Mater.* **235**, 118066 (2022).
63. Zhang, J. et al. Enhanced contact performance and thermal tolerance of $\text{Ni}/\text{Bi}_2\text{Te}_3$ Joints for Bi_2Te_3 -Based thermoelectric devices. *ACS Appl. Mater. Interfaces* **15**, 22705–22713 (2023).
64. Shi, W. et al. Batch fabrication and interface stabilization accelerate application of skutterudite thermoelectric module for power generation. *Adv. Energy Mater.* **14**, 2303698 (2024).
65. Qu, N. et al. Interfacial design contributing to high conversion efficiency in $\text{Mg}_3(\text{Sb}, \text{Bi})_2/\text{Bi}_2\text{Te}_3$ thermoelectric module with superior stability. *Adv. Energy Mater.* **14**, 2302818 (2024).
66. Liu, Z., Mao, J., Sui, J. & Ren, Z. High thermoelectric performance of α -MgAgSb for power generation. *Energy Environ. Sci.* **11**, 23–44 (2018).
67. Li, S. S. in *Semiconductor Physical Electronics* (ed Sheng S. Li) 284–333 (Springer, 2006).
68. Taylor, P. J. et al. Controlled improvement in specific contact resistivity for thermoelectric materials by ion implantation. *Appl. Phys. Lett.* **103**, 043902 (2013).
69. Liang, Z. et al. Composition-dependent contact resistivity in an n-type $\text{Mg}_3\text{Sb}_x\text{Bi}_{2-x}$ thermoelectric single leg. *Mater. Today Energy* **29**, 101099 (2022).
70. Matula, R. A. Electrical resistivity of copper, gold, palladium, and silver. *J. Phys. Chem. Ref. Data* **8**, 1147–1298 (1979).
71. Wikipedia contributors. Prices of chemical elements. *Wikipedia, The Free Encyclopedia*. https://en.wikipedia.org/wiki/Prices_of_chemical_elements/ (2025).
72. Chetty, R., Babu, J. & Mori, T. Best practices for evaluating the performance of thermoelectric devices. *Joule* **8**, 556–562 (2024).
73. Wu, X. et al. Interface and surface engineering realized high efficiency of 13% and improved thermal stability in $\text{Mg}_3\text{Sb}_{1.5}\text{Bi}_{0.5}$ -Based thermoelectric generation devices. *Adv. Energy Mater.* **12**, 2203039 (2022).
74. Yin, L. et al. Low-temperature sintering of Ag nanoparticles for high-performance thermoelectric module design. *Nat. Energy* **8**, 665–674 (2023).
75. Jiang, M. et al. High-efficiency and reliable same-parent thermoelectric modules using Mg_3Sb_2 -based compounds. *Natl. Sci. Rev.* **10**, nwad095 (2023).
76. Kresse, G. & Furthmüller, J. Efficient iterative schemes for ab initio total-energy calculations using a plane-wave basis set. *Phys. Rev. B* **54**, 11169–11186 (1996).
77. Kresse, G. & Joubert, D. From ultrasoft pseudopotentials to the projector augmented-wave method. *Phys. Rev. B* **59**, 1758–1775 (1999).
78. Perdew, J. P., Burke, K. & Ernzerhof, M. Generalized gradient approximation made simple. *Phys. Rev. Lett.* **77**, 3865–3868 (1996).
79. Tran, F. & Blaha, P. Accurate band gaps of semiconductors and insulators with a semilocal exchange-correlation potential. *Phys. Rev. Lett.* **102**, 226401 (2009).
80. Wang, V., Xu, N., Liu, J.-C., Tang, G. & Geng, W.-T. VASPKIT: a user-friendly interface facilitating high-throughput computing and analysis using VASP code. *Comput. Phys. Commun.* **267**, 108033 (2021).

Acknowledgements

This work was supported by JST Mirai Program (JPMJMI19A1, T.M.).

Author contributions

A.L. and T.M. designed the project. A.L. prepared the samples and carried out the transport measurements and conversion efficiency measurement. L.W. and J.L. provided the samples of $\text{Mg}_3(\text{Sb},\text{Bi})_2$ and MgCuSb . A.L. analyzed the data and wrote the original manuscript. T.M. supervised the whole project. A.L., L.W., J.L., X.W., and T. M. discussed, reviewed and edited the manuscript.

Competing interests

T.M. and A.L. have filed one Japanese patent application (2024–204680) on the work described here. The remaining authors declare no competing interests.

Additional information

Supplementary information The online version contains supplementary material available at <https://doi.org/10.1038/s41467-025-56861-3>.

Correspondence and requests for materials should be addressed to Takao Mori.

Peer review information *Nature Communications* thanks Jamal-Deen Musah, and the other, anonymous, reviewer(s) for their contribution to the peer review of this work. A peer review file is available.

Reprints and permissions information is available at <http://www.nature.com/reprints>

Publisher's note Springer Nature remains neutral with regard to jurisdictional claims in published maps and institutional affiliations.

Open Access This article is licensed under a Creative Commons Attribution-NonCommercial-NoDerivatives 4.0 International License, which permits any non-commercial use, sharing, distribution and reproduction in any medium or format, as long as you give appropriate credit to the original author(s) and the source, provide a link to the Creative Commons licence, and indicate if you modified the licensed material. You do not have permission under this licence to share adapted material derived from this article or parts of it. The images or other third party material in this article are included in the article's Creative Commons licence, unless indicated otherwise in a credit line to the material. If material is not included in the article's Creative Commons licence and your intended use is not permitted by statutory regulation or exceeds the permitted use, you will need to obtain permission directly from the copyright holder. To view a copy of this licence, visit <http://creativecommons.org/licenses/by-nc-nd/4.0/>.

© The Author(s) 2025